

# Three-Dimensional Imaging by Deconvolution Microscopy

James G. McNally,\* Tatiana Karpova,\* John Cooper,†  
and José Angel Conchello‡

\*Laboratory of Receptor Biology and Gene Expression, NCI/NIH, Bethesda, Maryland 20892;  
and †Department of Cell Biology and ‡Institute for Biomedical Computing,  
Washington University, St. Louis, Missouri 63110

---

Deconvolution is a computational method used to reduce out-of-focus fluorescence in three-dimensional (3D) microscope images. It can be applied in principle to any type of microscope image but has most often been used to improve images from conventional fluorescence microscopes. Compared to other forms of 3D light microscopy, like confocal microscopy, the advantage of deconvolution microscopy is that it can be accomplished at very low light levels, thus enabling multiple focal-plane imaging of light-sensitive living specimens over long time periods. Here we discuss the principles of deconvolution microscopy, describe different computational approaches for deconvolution, and discuss interpretation of deconvolved images with a particular emphasis on what artifacts may arise. © 1999 Academic Press

---

Most three-dimensional (3D) fluorescence microscopy is now done using a confocal microscope (1). Confocal microscopes are better than conventional fluorescence microscopes because the confocal design reduces haze from fluorescent objects not in the focal plane. This out-of-focus haze contributes significantly to background, and so its removal improves image contrast. With clearer focal-plane images, it becomes practical to acquire a three-dimensional image stack. This stack is the optical equivalent of a series of microtome slices, permitting a 3D reconstruction of a specimen.

Although confocal microscopy has many advantages, it does have limitations. A serious drawback for some applications is the amount of excitation light required to produce a confocal image. This may be a problem for fixed specimens that require many focal-plane images or for fixed specimens that are labeled with several different dyes. In these cases, the excitation-light dosage required to obtain satisfactory 3D images may

bleach the dye. This sensitivity issue is especially critical when living specimens are examined. In this case, specimen viability as well as bleaching become serious concerns.

These limitations in sensitivity have placed constraints on what can be accomplished by confocal microscopy, particularly for long-term 3D imaging of living specimens. Time-lapse studies are often of interest to observe changes in the distribution of a molecule or movements of organelles within a cell. Often it is desirable, if not essential, to follow these changes in 3D, for example to track objects that move from one focal plane to another. In many applications, it is also advisable to collect many, closely spaced focal planes because this provides improved resolution of the image in the third dimension ( $Z$ ). Ideally,  $Z$  resolution should be close to the resolution obtained within the focal plane, and so for high  $Z$  resolution, 100 or more focal planes might well be necessary to span the full depth of a specimen. All of these requirements add up to a considerable light dosage. A 3D time-lapse sequence of 50 time points, with 50 focal planes per time point, would require 2500 images.

Such imaging requirements are met by a complementary approach to 3D microscopy, often referred to as deconvolution (also known as wide-field deconvolution, digital-imaging microscopy, digital confocal, computational optical sectioning, or exhaustive photon reassignment). Such approaches are now available commercially from several different manufacturers. Deconvolution microscope systems are cheaper than most confocal microscopes and collect data faster than most confocals. However, to produce a 3D image, the deconvolution approach requires computational processing that can take anywhere from seconds to hours.

In addition, interpretation of these images requires some knowledge of the processing methods such that a user can both recognize artifacts and identify real features. To aid potential users of this technique, this article explains the underlying principles of deconvolution and provides guidance in the choice of deconvolution methods and subsequent interpretation of the processed images.

## DESCRIPTION OF METHOD

### *The Principle of Deconvolution*

All forms of 3D fluorescence microscopy must confront a fundamental problem. The image formed by a conventional fluorescence microscope contains light from throughout the specimen. This “out-of-focus” fluorescence confounds determination of what is actually present in the focal plane. Reduction of out-of-focus light is the task of 3D microscopy. This reduction occurs in a confocal microscope by positioning a pinhole in front of the detector such that most of the light passing through the pinhole derives from the focal plane and not from surrounding regions.

Reduction of out-of-focus light occurs computationally in deconvolution microscopy. (To assist readers with the terminology used in this article, Table 1 should be consulted for definitions of some of the key words used in this field.) Deconvolution methods determine how much out-of-focus light is expected for the optics in use and then seek to redistribute this light to its points of origin in the specimen. The characterization of out-of-focus light is based on the 3D image of a point source of light, the so-called point-spread function (PSF). The image of a point source is never a point

source, even if a perfect lens were used. The reason is that the aperture of any lens is finite and therefore fails to collect all of the light emitted from the point source and consequently cannot form a perfect image. Instead, a 3D image results in the form of a double cone with tips meeting at the point source. An aperture also introduces diffraction leading to ring patterns modulating the double-cone structure of the PSF (Fig. 1).

The PSF can be used to characterize the image formation process in any specimen. At each location ( $X, Y, Z$ ) in a specimen, some number of fluorescent dye molecules is present, each cluster of molecules corresponding to a point source of light whose intensity is determined by the number of molecules in the cluster. The 3D sum of all these point-spread functions is the 3D image. In this 3D image, out-of-focus light arises from the summed contributions of many PSFs. In most images, all traces of the original diffraction ring patterns underlying the out-of-focus light are hidden due to the summation of so many PSFs. Nevertheless, multiple PSFs still underlie the final image. Using a knowledge of the PSF for the optics in use, deconvolution seeks to deduce the original distribution of point sources in a specimen that must have given rise to the image collected.

Deconvolution and, more generally, image restoration techniques have been applied to a variety of imaging scenarios, ranging from positron-emission tomography to telescope imaging. All of these modalities share an underlying property. An imaging process distorts an object. By characterizing this distortion, the image can be restored to a state more closely resembling the original object. This general picture applies not only to wide-field fluorescence microscopy but also to bright-field, Nomarski or even confocal microscopy.

**TABLE 1**  
Nomenclature

Term	Explanation
PSF	Abbreviation for the point-spread function, which is the 3D image of a point source
Algorithm	Computerized procedure to carry out a calculation
Deconvolution	Method to undo the degradations introduced by an imaging process; a microscopic image is described mathematically as the convolution of the PSF with the object; to retrieve the original object from the image data, deconvolution is required
Pixel	Abbreviation for picture element; the image is composed of a grid of picture elements, each with an intensity corresponding to the local intensity at that point in the specimen
Voxel	3D pixel, a volume element, incorporating the step size between focal planes as the third dimension; the 3D image is built from a 3D grid of voxels
$X, Y, Z$	Coordinates for a 3D image; $XY$ correspond to the focal-plane (or lateral) coordinates and $Z$ corresponds to the direction of focal-plane change (or axial) coordinates
Optical axis	$Z$ axis

Confocal microscopes have a PSF that is much narrower, particularly in  $Z$ , than that of a wide-field PSF. Still, the confocal PSF is not a point, and so confocal images can also be improved by deconvolution (2, 3).

### PSF Determination

An accurate PSF is an important ingredient for deconvolution. The PSF can be determined either experimentally or theoretically. As a consistency check, both approaches are advisable. It is wise to start with a theoretical determination to get an idea of what to expect experimentally, at least under ideal conditions. Software for PSF calculation is available with some commercial deconvolution packages or if not available it can be downloaded directly from the web (<http://www.ibt.wustl.edu/bcl/xcosm/xcosm.html>). The following information is normally required: numerical aperture of the objective (NA, listed on the lens housing), working distance of the objective (available from the manufacturer specifications), wavelength of the emitted light (typically the peak value in the emission filter's spectrum),  $XYZ$  dimensions of the PSF (typically the same dimensions as the data to be processed), size of a pixel (again typically the same as the  $XY$  pixel size of the image data), spacing between  $Z$  slices (also typically the same as the image data), refractive index of the immersion medium (usually available on the immersion oil bottle, or 1.33 for water, or 1.00 for air), and thickness of the coverslip (nominally 0.17 mm corresponding to a No. 1.5 coverslip; No. 0 and No. 1 coverslips are thinner and No. 2 is thicker; considerable variability exists even among coverslips of a given number but precise knowledge of coverslip thickness is critical only for non-oil lenses.) On entering these values, the PSF is computed usually in a matter of min-

utes. The resultant PSF can be viewed to confirm that it has the general structure seen in Figs. 1a and 1b. Much of the energy of the PSF is concentrated near its point of origin; so, when examining the full 3D structure of a PSF image, it is necessary to adjust the contrast levels dramatically, for example by using a logarithmic scale (Fig. 1) or by drastically compressing the contrast range (Figs. 4b, 4e, 4h, and 4k).

In addition to computing a theoretical PSF, it is advisable to measure a PSF for the optical conditions in use. The experimental approach is easy to comprehend but painstaking to carry out. As a point source, a fluorescent microsphere is used. These are commercially available from several sources, including Polysciences or Molecular Probes (Warrington, PA). To approximate a point source, the microsphere should be as small as possible but small microspheres are difficult to visualize and bleach more rapidly. As a compromise, a microsphere diameter about one-third of the resolution size limit expected for the microscope objective in use should be chosen. With this criterion, the microsphere is smaller than the minimum distance that can be resolved. The Rayleigh resolution limit is  $1.22\lambda/\text{NA}$ , where  $\lambda$  is the wavelength of emitted light. The formula for the recommended microsphere diameter is one-third of this value, or  $0.41\lambda/\text{NA}$  (4). For an NA = 1.4 objective operating with green fluorescence ( $\lambda = 500$  nm), a microsphere diameter of  $0.15 \mu\text{m}$  is recommended.

How should the microsphere be imaged? Ideally, measurement of the PSF should be made under conditions approximating those in the actual specimen. In principle, this requires injection of the microspheres into the specimen and then measuring the PSF *in situ*.

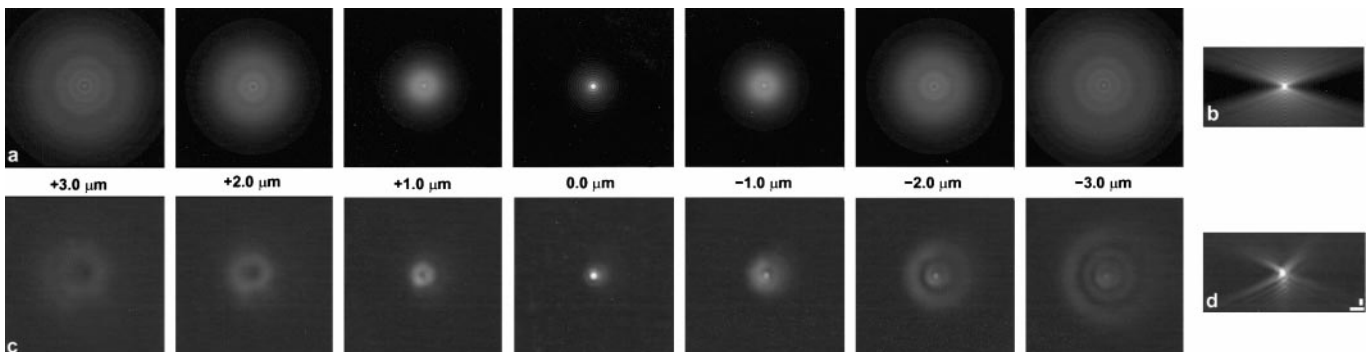


**FIG. 1.** Sequential focal planes through a theoretically predicted (a) or experimentally determined (b) point-spread function (PSF) for a  $100\times$ , 1.35 NA Olympus UplanApo objective. Distances above and below focus are shown from  $+3.0 \mu\text{m}$  to  $-3.0 \mu\text{m}$ . Observe that for the theoretical PSF (a) rings increase in number and grow in diameter as the point source is imaged above or below focus ( $0.0 \mu\text{m}$  corresponds to in focus). Ring patterns in (a) are symmetrical at equal distances above and below focus, whereas for the experimental PSF (c), ring patterns are more pronounced below focus. When viewed from the side (an  $XZ$  view), the PSF forms a double cone (b, theoretical PSF; d, experimental PSF). The edge of the cone corresponds to the increasing ring size as the microscope focal plane moves further away from the point source. The presence or absence of symmetry in ring patterns is also evident in the  $XZ$  view. For the experimental PSF (d), this asymmetry in ring patterns arises from spherical aberration, most likely a defect in this particular objective. Intensities in a–i are displayed on a logarithmic scale to highlight the weak outer rings of the PSF. Bars:  $1 \mu\text{m}$ .

This is difficult; so, PSFs are typically measured by drying microspheres on a coverslip. The microsphere concentration should be low enough to yield a density of microspheres on the coverslip surface such that the out-of-focus rings from one microsphere do not intersect out-of-focus rings from neighboring microspheres. If a coverslip of 0.17 mm thickness (typically found in a collection of No. 1.5 coverslips) and the proper immersion medium are used, then the imaging conditions are ideal in that they replicate those for which the microscope objective was designed. If other imaging conditions are used for the real specimen, such as different immersion medium, or if the specimen is not in direct contact with the cover slip, then such modifications should be replicated as closely as possible during PSF measurement. These nonideal imaging conditions adversely affect the PSF and therefore degrade image quality. They should be avoided as much as possible when setting up the actual specimen but if that is not feasible, then the PSF measurement should account for the specimen-imaging conditions.

Once an isolated microsphere is found, a 3D image is acquired using the same pixel size in  $XY$  and the same step size in  $Z$  as for the real specimen. The measurement may be repeated several times and then averaged to reduce noise, assuming bleaching is not significant. Bleaching may be deterred by embedding the beads (after they have dried on the coverslip) in an optical cement or a medium that incorporates an antifade agent.

Once a PSF measurement has been made (Figs. 1c and 1d), it should be used first and foremost to assess the quality of the microscope optics and to improve them if possible. The best optics yield PSFs that are symmetrical in  $Z$  and diffraction ring patterns that are circularly symmetric. When the PSF is asymmetrical, optical aberrations are present (see for example Figs. 1c and 1d). These may be identified and potentially corrected by interchanging optical elements, such as lenses and dichroic mirrors, in order to determine which components are principally responsible for the asymmetry. In some cases, small changes in immersion oil refractive index yield improved PSFs (5). For optimal deconvolution, it is best to troubleshoot a microscope system for PSF asymmetries because aberrations in the system limit achievable resolution. Aberrations can be ameliorated by deconvolution but the ultimate resolution is still limited in the presence of aberration and such aberrations should be corrected whenever possible to obtain the best deconvolved images of the real specimen.

The measured PSF of an optimized system can now be compared to the theoretical PSF. Any residual asymmetries in the experimental PSF should be noted. Often some spherical aberration is present in the system (5). This manifests as a shape difference between

the top and bottom cones of the PSF (Fig. 1d). In the extreme, an  $XZ$  profile of the PSF is “Y”-shaped instead of “X”-shaped (Fig. 4k). Whatever differences exist between the two PSFs should be noted, and then both the measured and experimental PSFs can be used for deconvolution (6). The measured PSF is likely to account better for the optics in use but the theoretical PSF has the advantage that it is noise free. In some cases (especially with high-NA lenses) (5), experimental PSFs have been found superior. In other cases, theoretical PSFs have done as well (especially with low-NA lenses) (6).

In comparing reconstructions with different PSFs it is useful to examine images not only in  $XY$  cross sections but also in  $XZ$ . The  $XZ$  view helps determine whether the PSF used did not correctly account for spherical aberration. As noted above this aberration is often present to some degree in many objectives. In addition, actual imaging conditions typically introduce this aberration even if the objective lens is aberration free. For example, imaging at some depth into a specimen invariably introduces some spherical aberration. Thus, this feature is often not accounted for in either a measured or an ideal theoretical PSF. This problem can be detected by examining the  $XZ$  view of the reconstructed image. If objects are asymmetrical in  $Z$ , then such a problem likely exists. It can sometimes be corrected by introducing spherical aberration into the PSF measurement or PSF calculation (see Interpretation of Deconvolved Images and Fig. 4).

### *Image Preprocessing*

Once an accurate PSF has been determined, 3D images of a specimen can be collected and prepared for deconvolution to remove systematic errors in data collection (7). All deconvolution methods assume that specimen illumination is spatially and temporally uniform but in reality this is rarely true. To correct for uneven spatial illumination of a specimen and uneven sensitivity of the camera, the image data are “flat-fielded.” Flat-fielding is beneficial, especially if a cooled scientific-grade charge-coupled device (CCD) camera is not used. Even for cooled CCD cameras, flat-fielding is typically beneficial for images in which neighboring wells in the camera are not averaged (a process known as binning). Flat-fielding software is usually available with commercial deconvolution packages. Flat-fielding is done by imaging a uniformly fluorescent object (such as fluorescent plastic) and then using the fluctuations in this image to calibrate the uneven illumination. This measurement also accounts for variable sensitivity in different regions of the camera. The flat-fielded image is then used as the basis to correct recorded intensities in the image of the actual specimen. Flat-fielding sometimes offers only marginal improvement, and so it may be advisable to compare deconvolved images with and

without flat-fielding to determine if this correction is worth the effort.

Cosmic rays can be another source of spatial fluctuation in images. These can be recognized as 1- to 2-pixel-wide hot spots that appear in just one focal plane. These hot spots typically completely saturate the camera intensity range and are therefore much brighter than any surrounding pixels. Such cosmic ray events are infrequent but are sometimes found in long time-lapse runs. If such hot pixels are not removed, problems can arise during deconvolution. In addition, hot pixels wreak havoc with movies produced from a time-lapse sequence. Time points with hot spots have a much broader intensity range than all other time points, and when images from such time points are scaled for display, the objects of interest are much dimmer than at all other time points. Fortunately, simple programs can be used to identify hot pixels and replace them with the average intensity of surrounding pixels.

The other form of inhomogeneous illumination is temporal due to excitation lamp flicker. Several options are available to reduce this effect. Flicker can often be improved simply by replacing an old mercury arc bulb with a new bulb. Better still is to replace a mercury arc lamp with a xenon lamp, which is fundamentally more stable. One drawback here is that green light in the xenon spectrum is not as bright as in the mercury spectrum. Correction for flicker can also be done computationally by rescaling intensities in one focal plane such that the summed intensity in that focal plane exactly matches the summed intensity in adjacent focal planes. The validity of this approach stems from the fact that the wide-field microscope collects all of the specimen's light, regardless of which focal plane is imaged, and so the summed intensity in any focal plane should be a constant. The best correction for flicker is to divert a fraction of excitation light to a photon counter. This accurately determines the illumination in each focal plane, thereby permitting an appropriate rescaling of each focal plane.

### *Deconvolution Algorithms*

An algorithm is a procedure that follows a defined series of steps and is carried out on a computer. Deconvolution algorithms are derived from a mathematical formula which describes the imaging process on a microscope. In its simplest form, the formula for microscope-image creation incorporates two known quantities, namely the PSF ( $X, Y, Z$ ) and the measured 3D image,  $I(X, Y, Z)$ , and one unknown quantity, namely the actual distribution of light in the 3D specimen,  $S(X, Y, Z)$ . These terms are related by the imaging equation

$$I(X, Y, Z) = S(X, Y, Z) \otimes \text{PSF}(X, Y, Z), \quad [1]$$

where the symbol  $X$  represents the mathematical operation known as a convolution. The convolution essentially shifts the PSF so that it is centered at each point in the specimen and then sums the contributions of all these shifted PSFs. Both the PSF( $X, Y, Z$ ) and the  $I(X, Y, Z)$  can be determined, and so the process of solving for  $S$  has become known as deconvolution. Different deconvolution methods solve for  $S$  in different ways, yielding different deconvolution algorithms. This section describes in nonmathematical terms the underlying principles of the major approaches to deconvolution. A list of different methods with relevant references is given in Table 2.

In what follows, we summarize the basic principles of each of the methods listed in Table 2. There is no best method for deconvolution. As a general but not absolute rule, methods that require more computer time yield better reconstructed images. In some cases, speed may be critical, for example in evaluating images in near "real time" as they are collected on the microscope or when large amounts of data are collected, as in a long time-lapse experiment in which long processing times for each time point become prohibitive. It is always advisable to test several different deconvolution algorithms. Any one feature of an image is often optimized by a particular algorithm, although the feature should be visible after processing by most if not all methods. As an example of the use and comparison of several different deconvolution methods, readers should consult Karpova *et al.* (8), in which three of the methods in Table 2 were used in parallel. Readers should also note that although a particular method in Table 2 is sometimes available from more than one source, there are always differences between implementations of a method, and so not all methods of the same type will necessarily yield the same results. Before purchasing a deconvolution package, there is no substitute for generating sample data sets and processing them with all of the methods under consideration.

**TABLE 2**  
Deconvolution Methods

Method	Reference
No neighbors	13
Nearest neighbors	14, 15
Linear methods	
Wiener filter, inverse filtering	16, 17
Linear least squares (LLS)	18
Constrained iterative	
Jansson van Cittert	14
Nonlinear least squares	19
Statistical image restoration	
Maximum likelihood	20–22
Maximum a posteriori	24
Maximum penalized likelihood	21, 22
Blind deconvolution	25, 26

The following summaries are designed as a guide to potential users who wish to assess the level of sophistication of any particular method.

*No neighbors.* Some of the simplest approaches to deconvolution actually ignore the imaging formula altogether (and therefore are not properly called deconvolution). These approaches use the information in only a single focal plane, and so the method must be independently applied to each focal-plane image. Such two-dimensional (2D) methods are based on the principle that out-of-focus light or blur tends to be “flatter” than the in-focus light from which it was derived. In a more rigorous sense, “flatter” means that the out-of-focus light tends to be composed of lower spatial frequencies (i.e., the light intensity varies slowly over the field of view). Thus, the simple 2D methods work by boosting only the higher spatial frequencies in the specimen. This approach can be reasonably effective for certain types of specimens that tend to be composed of mostly higher spatial frequencies, i.e., components that vary rapidly in  $XY$ , like puncta or filaments. For such specimens, removing lower spatial frequencies removes mostly out-of-focus light, and this leaves the objects of interest. A significant advantage of this approach is its speed. Clearly, however, most specimens are a complex mixture of low and high spatial frequencies, and so these 2D filtering methods run the risk of removing components of interest within the specimen.

*Nearest neighbors.* The next simplest approaches to deconvolution incorporate some but not all of the 3D information. These approaches use information from only adjacent focal planes and so are often referred to as nearest-neighbor deconvolution. This approach makes use of the imaging formula described above but instead of summing out-of-focus light contributions from all the focal planes in the specimen, only two are considered, one above and one below the plane of interest. By subtracting the blur expected from adjacent planes from the focal plane, one removes some amount of blur in the focal plane image. There are two approximations in this method which compromise results. First, the image in any one focal plane contains out-of-focus light from all other focal planes, although the strongest contributions typically do come from the adjacent planes. Second, the determination of the out-of-focus light contribution from adjacent planes is itself only an estimate in the nearest neighbors method, since this information is unknowable without solving the full 3D problem. The chief advantage of this approach is that it is extremely fast to compute. With modern workstations however, more sophisticated methods, such as the linear methods described next, can also yield results in a matter of seconds.

*Linear methods: inverse filtering, Wiener filters, linear least squares.* The simplest true 3D methods for deconvolution use the information from all focal planes

and attempt to directly solve the imaging equation (Eq. [1]) described above. This equation can be converted to a simple multiplication by Fourier transforming both sides and in principle solved for the Fourier transform of  $S$  as follows:

$$S = I/PSF, \quad [2]$$

(where italicized letters indicate the Fourier transform). It turns out (see below) that this deceptively simple equation is confounded by the presence of noise in the image. Intuitively, the complexities introduced by noise can be understood by considering again that deconvolution methods seek to restore out-of-focus light to its points of origin. When these methods encounter a given intensity of light at a pixel in an image, they must reconcile the relative contributions of in-focus and out-of-focus light at that point. Without noise this can be done by a self-consistency argument resulting in Eq. [2] above but when noise is present, an unknown, random component is added to the problem.

In the Fourier method described by Eq. [2], noise in the measured data becomes a serious problem at values where the denominator ( $PSF$ ) is very small or zero. It turns out that the denominator is always small at high spatial frequencies in the image (e.g., very sharp edges). Intensities in the measured image are also very small at these same higher spatial frequencies (because the Fourier transform of the  $PSF$  modulates intensity levels in the measured image), and so noise dominates at these values, leading to an inaccurate result for  $S$ . To address this problem, all Fourier approaches to deconvolution adopt some strategy to reduce noise amplification. All essentially strike a compromise by reducing the contributions of high spatial frequencies to the image, thus reducing the deleterious effects of noise, but also reducing sharpness in the image. Consequently, these methods typically have at least one variable parameter that regulates how much high frequency noise is eliminated. For each specimen, a user must therefore determine the tradeoff between image sharpness and noise amplification.

*Constrained iterative methods: Janson-van Cittert, nonlinear least squares.* Although the linear methods described above are fast to compute, they have several drawbacks. A significant one is that intensities can be negative in the deconvolved image. Negative intensities confound any sort of quantitative analysis, and even for a qualitative analysis, negative intensities generate artifacts (see Interpretation of Deconvolved Images). Therefore, a number of deconvolution methods impose the constraint that image intensities be positive. More generally, a positivity constraint should yield better images by providing additional information to help a deconvolution method dissect out the

differences among in-focus light, out-of-focus light, and noise.

The constrained iterative methods are no longer one-step procedures like the linear methods described above. Rather, some calculation is repeated many times as a solution to the problem is gradually approached. Such methods are called iterative and require more computational time. Iterative methods typically converge to a solution after some number of steps. The time to convergence depends on how many iterations are required to converge, as well as the time required to compute each iteration. For the two constrained iterative methods noted here, the number of iterations required may vary from 10 to 200, and the computation time per step is that required to perform two 3D fast Fourier transforms.

*Statistical image restoration: maximum likelihood, maximum a posteriori probability, maximum penalized likelihood.* In addition to a positivity constraint, the statistical image restoration methods add still more information to the deconvolution method. Specifically, these methods incorporate information about the statistics of the noise present during imaging. In principle, this additional information should further help in the process of dissecting out the differences among in-focus light, out-of-focus light, and noise. With the introduction of a model for the noise in the imaging process, these deconvolution methods are often called image restoration procedures because they seek to restore degradations introduced not only by the optics but also by the noise. As might be expected, such methods can be especially valuable in cases in which the fluorescent signal is weak and noise is a significant component in the image. In addition, these methods are capable of recovering certain information not passed by the objective lens (see discussion of the elongation artifact under Interpretation of Deconvolved Images and Conchello (9)).

The image restoration methods are also iterative and typically require many more iterations than the constrained iterative methods (from 100 to 3000). The time required per iteration is also about twice as long as that of the constrained iterative methods. Thus, these methods often require several hours to overnight to compute a satisfactory image. For many specimens however, these methods are superior.

*Blind deconvolution.* Regardless of how effective any of the preceding deconvolution methods are, if they are given an inaccurate PSF the deconvolved image will suffer. Yet, a truly accurate determination of the PSF is nearly impossible for any real imaging situation. This is because noise is always introduced in a PSF measurement. Even if a theoretical PSF is used, it cannot completely account for subtle aberrations present in any optical system. Moreover, in a real imaging situation, the true PSF is not represented by a

point source resting on a cover slip but rather should be represented by a point source within a specimen. Such a PSF is virtually impossible to measure and at best difficult to estimate theoretically.

In this sense the PSF can also be viewed as an unknown in the deconvolution problem. Accordingly, certain methods seek to estimate not only the original image but also the PSF for the optics in use. In so doing, these “blind deconvolution” methods hold promise for a more accurate determination of the original image because they are not in any way constrained by an inaccurate PSF. Such methods, however, face a more considerable challenge, in that there is even less information supplied to solve the deconvolution problem. Nonetheless, such methods can produce excellent deconvolved images. This approach is also iterative and so is slower than the simple linear methods.

#### Interpretation of Deconvolved Images

If deconvolution is successful, then a number of improvements in the image should be noted (Fig. 2). These include improved contrast and reduced background haze. In addition, deconvolution should make

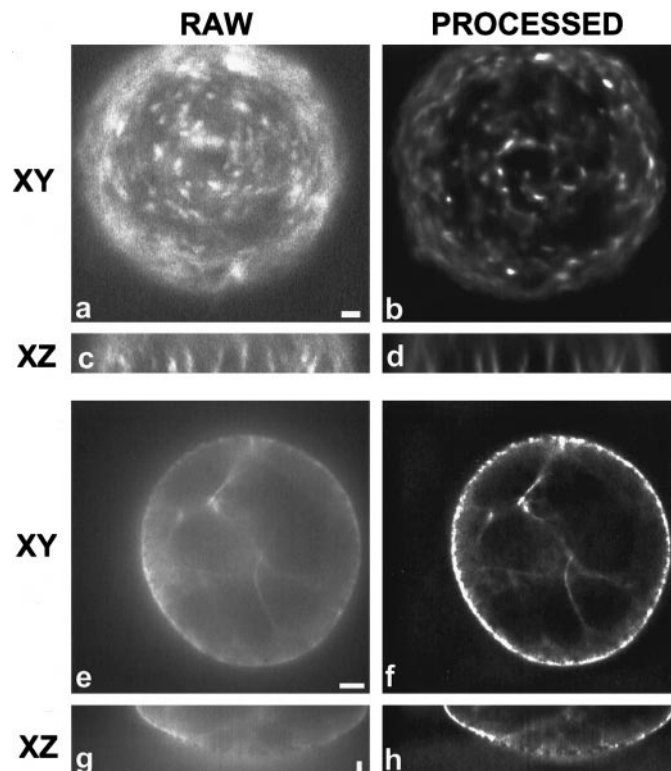


**FIG. 2.** Example of effective deconvolution. Top: Raw (a,c) and processed (b,d) images of GFP-tagged *Dictyostelium* cells within a cell mass. Bottom: Raw (e,g) and processed (f,h) images of GFP-tagged movement protein in BY2 tobacco protoplasts (27). Note that considerable haze is removed after processing. Image contrast is enhanced and the edges of bright objects are sharper. Bars: 20  $\mu\text{m}$  (a–d), 5  $\mu\text{m}$  (e–h).

the edges of objects sharper. The spread of objects in the  $Z$  direction should also be reduced, and this should be most apparent when images are examined in  $XZ$  cross section.

Even with an accurate PSF and an effective deconvolution algorithm, deconvolved images can suffer from a variety of defects and artifacts. It is vital for users to be aware of the sorts of artifacts that can arise and what can be done to ameliorate them or when that is not possible, to know to ignore them. In evaluating any potentially important structure in a deconvolved image, the bottom line is to be certain that some trace of the structure is present in the raw, unprocessed data. Following deconvolution, the structure should become brighter and sharper and more readily apparent in the deconvolved image but if the structure of interest resembles any of the artifacts described below, then extreme care must be used in interpretation. In addition, it is always prudent to apply several different deconvolution methods to demonstrate that the structure of interest is present after application of each method, although one method is likely to show the structure more clearly than another, and some less sophisticated methods may be unable to resolve certain structures. Some of the most common artifacts and defects in deconvolved images are described below.

A very common defect is alternating bright and dark stripes in a deconvolved image viewed in  $XZ$  (Fig. 3).

One reason that these stripes can arise is that flicker from the excitation light source has not been completely corrected (see Image Preprocessing). If some excitation-light flicker corrupts the raw data, it is often exaggerated by deconvolution.

Even if there is no lamp flicker, stripes can arise in  $XZ$  when not enough out-of-focus light has been collected either above or below the region of interest (Fig. 3). Such "truncated" raw data do not provide enough out-of-focus light for certain algorithms (particularly the linear algorithms) to adequately solve the deconvolution equation. Ideally, one should collect as much out-of-focus light as possible, thereby providing the deconvolution method with as much information as possible. If stripes are present in  $XZ$  and there are bright objects in planes near the top or bottom of the raw image stack, then a larger 3D volume should be used, if at all possible.

Other periodic patterns may also arise following deconvolution, again most commonly with the linear methods. These so-called ringing artifacts typically appear around bright objects in the image and take the form of concentric bright rings surrounding the bright object (Fig. 3b). These patterns can be dissipated to some degree by modifying tuning parameters in the deconvolution method but, if possible, an alternative deconvolution method should be tried to eliminate this artifact.

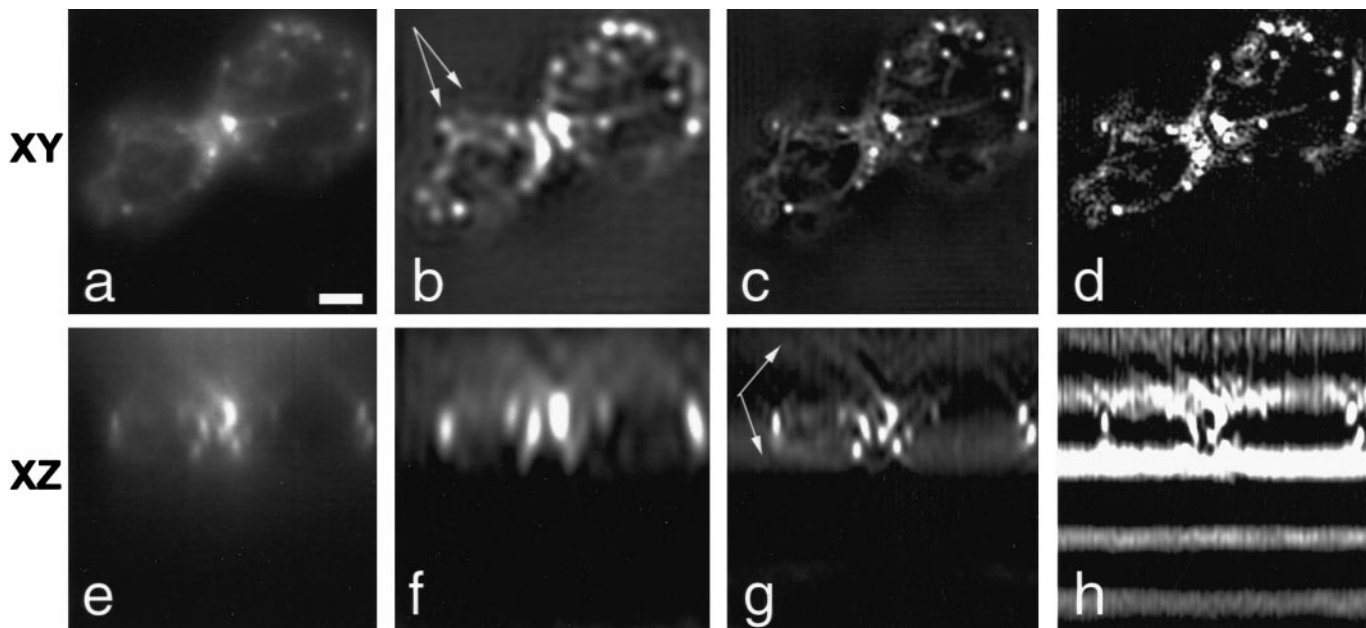


**FIG. 3.** Ringing and stripe artifacts after processing by a linear method. Shown are  $XY$  and  $XZ$  views of yeast cells stained with rhodamine phalloidin. An unprocessed image is displayed in (a,e). Subsequent images (b–d,f–h) are processed by a linear deconvolution method (LLS) (18) at three different parameter settings. As the LLS parameter changes in b–d and f–h, image sharpness improves but graininess and noise also increase. Arrows in b indicate one common artifact of linear methods, namely ringing, in this case around the outer edge of the yeast cell. Arrows in g indicate a second artifact, namely the appearance of two stripes. Stripes are further accentuated (h) by changing the algorithm's tuning parameter to an excessive level. The stripe artifact may arise in these images because in the original, raw data not all of the out-of-focus light has been captured above the image (e). Bar: 2  $\mu\text{m}$ .



Another common defect in deconvolved images is PSF mismatch (with the notable exception of blind deconvolution). This was already discussed under PSF Determination. The defect manifests most typically as an asymmetry of objects within the deconvolved image when viewed in  $XZ$  (Fig. 4). The specific asymmetry is

that objects viewed in  $XZ$  exhibit more out-of-focus light emanating from either their top or their bottom (Fig. 4f). This often arises because the PSF used does not account for the specific imaging conditions in the specimen, in particular if the region of interest in the specimen is at some depth and there is a refractive

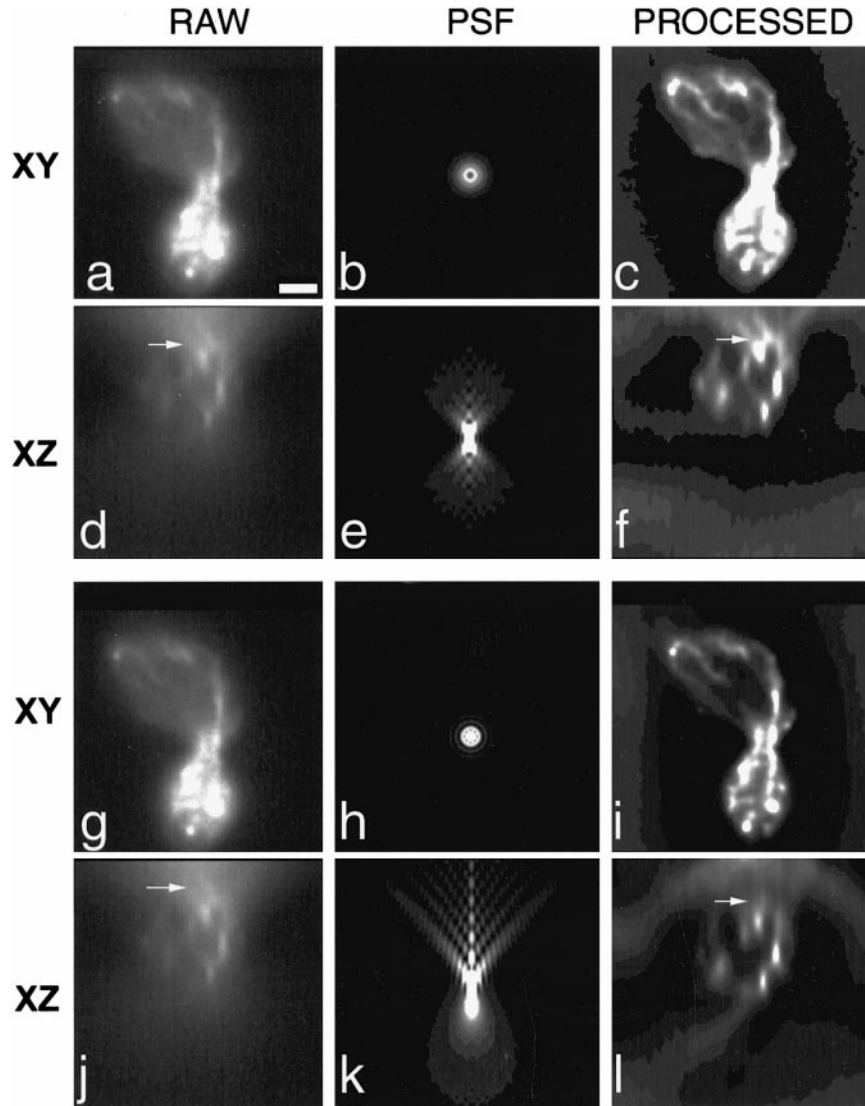


**FIG. 4.** Correction of spherical aberration in an image by using a spherically aberrant PSF. Unprocessed images of actin-stained yeast cells (a,d) exhibit evidence for some spherical aberration. This manifests in an  $XZ$  view (d) as more light spreading above (arrow in d) than below fluorescent spots in the image. As a consequence, the spots exhibit more of a “Y-shaped” profile in  $XZ$  view. The theoretically determined PSF for the objective used ( $60\times$ , 1.4 NA) is aberration free and exhibits an “X-shaped” symmetry in an  $XZ$  view (e). When this PSF is used to process the raw data, not enough light is removed from above the bright objects, leaving residual “V-shaped” tails (arrow in f). (The images in c,f,i,l are displayed on a very compressed contrast scale to highlight the residual tails. As a consequence, there are few gray levels available in the images, and so contrast contour lines are visible.) The imaging conditions for the yeast cell are not ideal, since an oil immersion objective was used to image at a depth of up to  $5\ \mu\text{m}$  into a watery cell. This mismatch of refractive index introduces spherical aberration. Such spherical aberration can be modeled theoretically by accounting for imaging depth into a watery specimen. The resultant PSF (k, computed for imaging at a depth of  $4\ \mu\text{m}$  into a medium of refractive index  $n = 1.33$ ) exhibits the “Y-shaped” profile characteristic of spherical aberration. When the same unprocessed data (shown again in g,j) are processed with this modified PSF, the spread of light above the bright objects is significantly reduced (arrow in l). Characteristic of spherical aberration, the in-focus plane or “plane of least confusion” in the PSF shifts compared to an aberration-free image. This can be seen in the  $XY$  PSF images which are taken at the same distance above the point source location but are clearly different (compare b and h). This  $Z$  shift in the PSF results in a  $Z$  shift in the processed image. In this case, the  $XZ$  view is lowered in panel l compared to panel f. Bar:  $2\ \mu\text{m}$ .

index mismatch between the immersion medium and the specimen. Using a water-immersion objective to collect images may help alleviate the problem, since the refractive index mismatch is smaller between specimen and water than between specimen and oil. It is also possible to simulate the actual imaging conditions in the specimen by determining a PSF from beads embedded at various depths in a water-based mounting medium. Use of these PSFs may improve the asymmetry in the deconvolved images. Finally, theoretical PSFs can also be computed by altering the depth and/or refractive index of the specimen (Fig. 4k). These can likewise be used in the deconvolution. Successful matching of the true PSF should produce objects in a deconvolved image that show equal elongation above and below their center as seen in an *XZ* view (Fig. 4).

Even with proper PSF matching, a symmetric *Z* elongation of objects remains following deconvolution of most objects by most algorithms (Fig. 5). This so-called elongation artifact is a consequence of noncon-

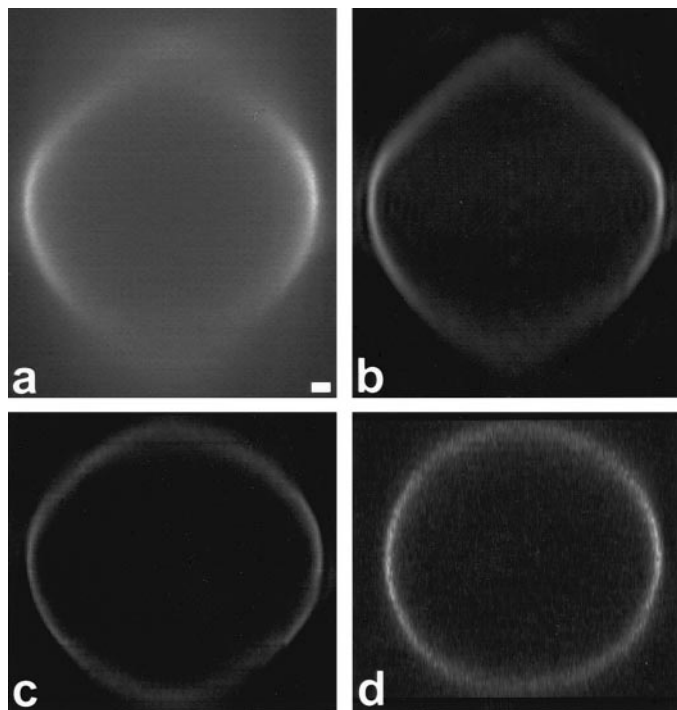


**FIG. 5.** Deconvolved images are often subject to an artifactual elongation in the *Z* direction. A raw image from a 15- $\mu\text{m}$  diameter bead is shown from an *XZ* view in (a). The bead is a spherical shell of fluorescence about 1  $\mu\text{m}$  thick. After processing by a linear method (LLS) (18), the bead exhibits an oblong profile in *XZ* (b). This is an artifactual elongation that arises due to limitations of wide-field microscopy (see text and Ref. 6) for an explanation of this phenomenon). This defect can be largely overcome by at least one deconvolution method, namely the maximum-likelihood expectation-maximization (EM) algorithm (9). Following several thousand iterations of this algorithm, the elongation in the *XZ* view is removed (ca., 3000 iterations), and the bead is in fact slightly compressed. Confocal images of a comparable bead in *XZ* view (d) do not exhibit the elongation artifact. Bar: 1  $\mu\text{m}$ .

focal imaging and is difficult to overcome using deconvolution on most images from a wide-field microscope (6). Some algorithms are more successful than others in reducing this elongation (Fig. 5c vs 5b) but the elongation is an intrinsic feature of wide-field imaging and a distinct disadvantage of this approach in comparison to confocal microscopy (Fig. 5d). The reasons for this difference between wide-field and confocal microscopy relate to the fact that a wide-field microscope collects all of the light from a specimen, while a confocal microscope collects light primarily from the focal plane. As a result, a wide-field microscope cannot localize the plane of focus for a uniform layer of dye because, regardless of whether the objective focuses on or above or below the layer of dye, the same amount of

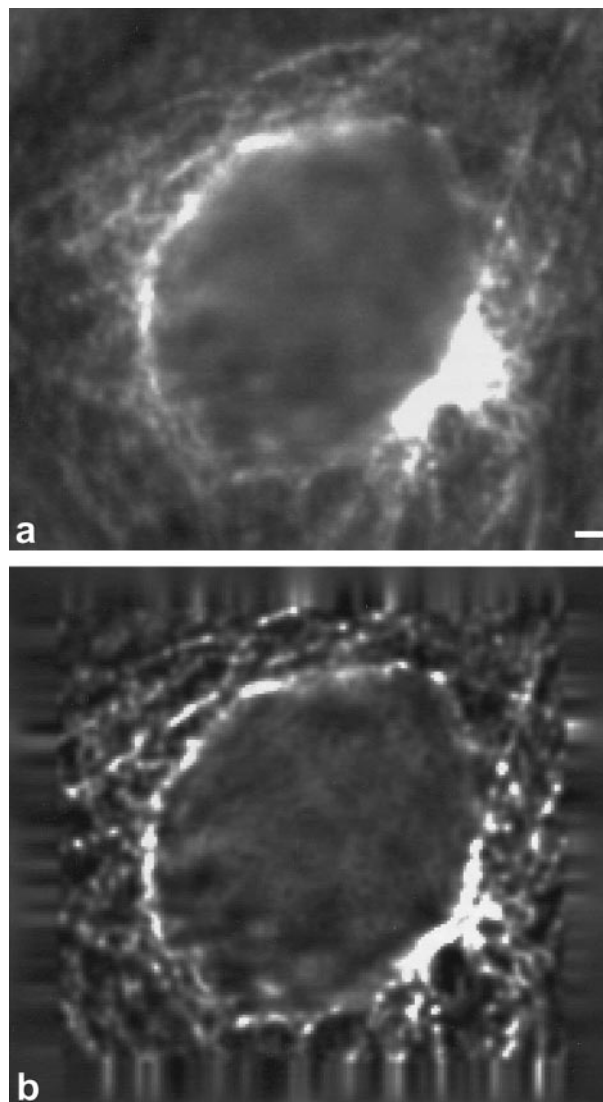


**FIG. 6.** Edge artifacts can also arise following deconvolution. Shown are raw (a) and processed (b) *XY* images of filaments in a plant cell. The outer frame of the processed image is distorted by deconvolution and should be ignored for data analysis. Bar: 1  $\mu\text{m}$ .

fluorescence is collected. Many real specimens are composed of regions which approximate a uniform layer of fluorescence, such as the top and bottom cap of the fluorescent bead shown in Fig. 5. Such regions are difficult to image by wide-field microscopy, and information from them is effectively lost during the imaging process.

Edge artifacts are another common defect of many methods. These are easily recognized as unusual features present at the edge of the 3D volume (Fig. 6).

They may appear, for example, as either brighter or blurrier regions framing the 3D volume. In any case, if potentially interesting structures are found at the edge of a deconvolved image, it is always advisable to reim-age the specimen such that the region of interest is centered in the 3D volume.

More subtle problems can arise with the combination of certain algorithms and certain 3D viewing tools. We have found (8) that filamentous structures (either actin or endoplasmic reticulum) could be lost in images pro-

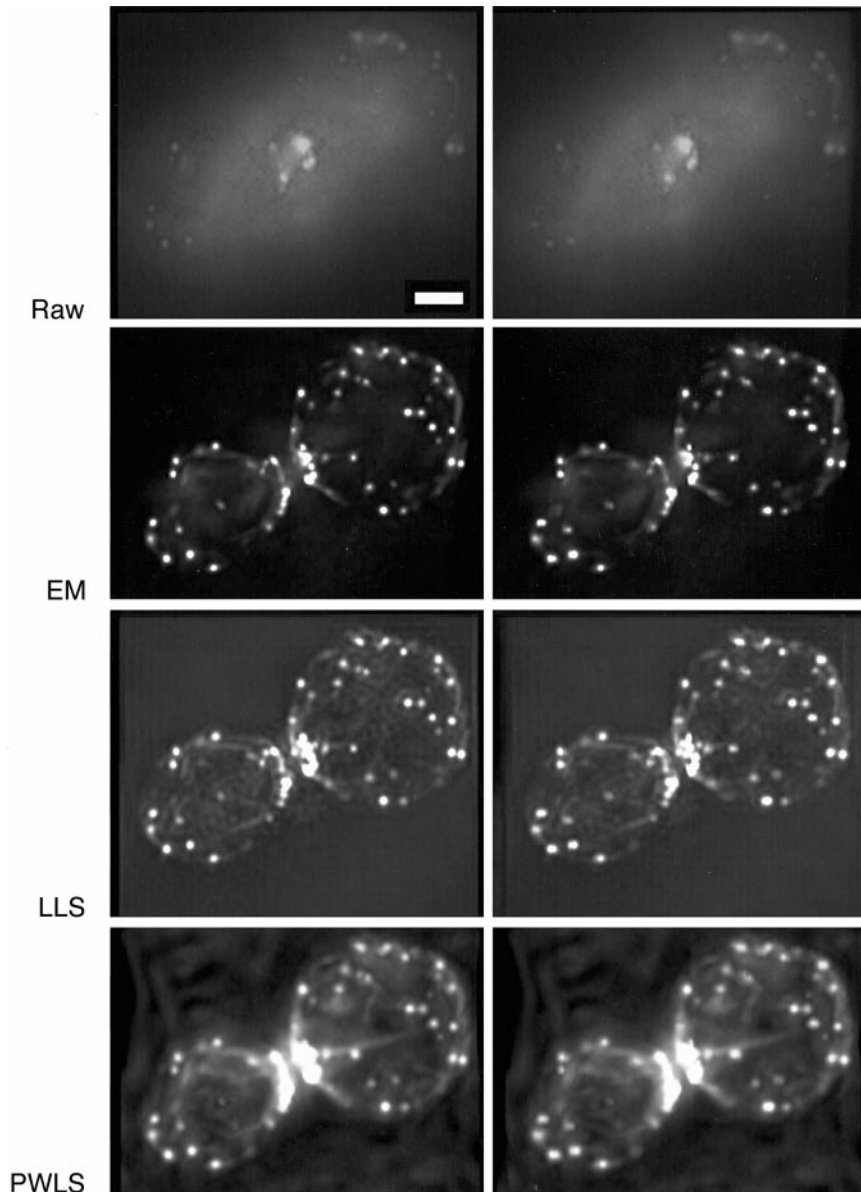


**FIG. 7.** Filaments can be difficult to visualize following deconvolution and stereo-pair projection. Stereo-pairs of 3D images of actin-stained yeast cells exhibit filamentous structure to varying degrees depending on the algorithm employed. The filaments cannot be seen at all in a stereo-pair of the raw data but can be easily visualized in individual sections of raw data (see Fig. 3a). When processed by the maximum-likelihood expectation-maximization (EM) algorithm and projected for stereo viewing, filaments are virtually absent. The same data processed by a linear method (LLS) exhibit clearer filaments when viewed in stereo but also exhibit ringing artifacts characteristic of such linear methods. The nonlinear iterative method of penalized weighted least squares (PWLS; J. Markham and J. A. Conchello, unpublished data) also preserves some filamentous structure when viewed in stereo, without introducing artifacts within the specimen. Bar: 2  $\mu\text{m}$ .

cessed by a maximum-likelihood EM algorithm and then viewed with a maximum-intensity projection (Fig. 7). Continuous filaments can appear fragmented in the projected image even though they can often be followed by stepping through the 3D volume of the deconvolved data and are readily apparent in the raw data. In this case, other deconvolution methods were better at retaining these structures.

### *Selecting a Deconvolution Microscope*

A deconvolution microscope can be assembled from individual components. This is time consuming but permits the most flexibility. Essential ingredients are a standard fluorescence microscope equipped with microstepping motor to control focus, a shutter to control the excitation light, and a cooled scientific-grade CCD camera with at least 12-bit resolution to collect images. An important feature of the CCD is its quantum efficiency, which reflects the percentage of incoming photons that are detected. Higher quantum efficiency indicates a more sensitive CCD. A second important CCD parameter is the read-out noise. Higher values here indicate less sensitivity. Finally, the readout rate of the CCD determines how fast images can be collected. Typically, there are trade-offs between the last two parameters. Faster CCDs generally have higher read-out noise. The best method to evaluate these different features is to test the camera with the specimen under study. To distinguish a dim specimen from background requires a camera with lower noise and higher quantum efficiency.

Several different, fully assembled commercial deconvolution microscopes are now available (see the recent review by Rizzuto *et al.* (10) for a partial listing of manufacturers). In selecting a commercial instrument, the same issues described above must be considered. In addition, commercial packages include one or two deconvolution methods, and these must be evaluated as well. If budget permits, it is advisable to purchase several different deconvolution packages from different manufacturers to allow for flexibility and to provide a consistency check. Deconvolution freeware is also available from the web (<http://www.ibr.wustl.edu/bcl/xcosm/xcosm.html>).

## CONCLUSIONS

Laser-scanning confocal microscopes are the workhorses of 3D microscopy but are not a cure-all for every 3D imaging need. There are now a number of alternatives to conventional laser-scanning confocal microscopy, including methods for faster scanning and multiple confocal aperture imaging, and new confocal designs continue to appear (11, 12). In addition, two-photon microscopy offers promise for imaging deep into

specimens and for longer-term imaging of living specimens.

One proven alternative to confocal imaging is 3D deconvolution. This approach offers some significant advantages, particularly when many focal-plane images are required, e.g., for time-lapse 3D imaging of living specimens, multiple labels within a single time point, or dyes that bleach rapidly. Commercial instruments are available; so, the technology is accessible. Some sophistication is required in interpreting these images but the method is a proven one for long-term 3D imaging studies. Moreover, images from any microscope, confocal or two-photon, can be further improved by deconvolution; so, the technique is widely applicable and should be considered as an adjunct to any form of 3D light microscopy.

## ACKNOWLEDGMENTS

We thank Patricia Clow for the *Dictyostelium* cell image of Fig. 2 and Scott Gens and Barbara Pickard for the plant cell image of Fig. 2.

## REFERENCES

- Pawley, J. B. (1995) *Handbook of Biological Confocal Microscopy*, Plenum, New York.
- Shaw, P. J. (1995) *in Handbook of Biological Confocal Microscopy* (Pawley, J. B., Ed.), pp. 373–387, Plenum, New York.
- Shaw, P. J., and Rawlins, D. J. (1991) *J. Microsc.* **163**, 151–165.
- Preza, C., Ollinger, J. M., McNally, J. G., and Thomas, L. J. (1992) *Micron. Microsc. Acta* **23**, 501–513.
- Hiraoka, Y., Sedat, J. W., and Agard, D. A. (1987) *Science* **238**, 36–41.
- McNally, J. G., Preza, C., Conchello, J.-A., and Thomas, L. J. (1994) *J. Opt. Soc. Am. A* **11**, 1056–1067.
- Chen, H., Swedlow, J. R., Grote, M., Sedat, J. W., and Agard, D. A. (1995) *in Handbook of Biological Confocal Microscopy* (Pawley, J. B., Ed.), pp. 197–210, Plenum New York.
- Karpova, T. S., McNally, J. G., Moltz, S. L., and Cooper, J. A. (1998) *J. Cell Biol.* **142**, 1501–1517.
- Conchello, J. A. (1998) *J. Opt. Soc. Am. A* **15**, 2609–2619.
- Rizzuto, R., Carrington, W., and Tuft, R. A. (1998) *Trends Cell Biol.* **8**, 288–292.
- Verveer, P. J., Hanley, Q. S., Verbeek, P. W., Van Vliet, L. J., and Jovin, T. M. (1998) *J. Microsc.* **189**, 192–198.
- Wilson, T., Juskaitis, R., Neil, M. A. A., and Kozubek, M. (1996) *Opt. Lett.* **21**, 1879–1881.
- Monck, J. R., Oberhauser, A. F., Keating, T. J., and Fernandez, J. M. (1992) *J. Cell Biol.* **116**, 745–759.
- Agard, D. A. (1984) *Annu. Rev. Biophys. Bioeng.* **13**, 191–219.
- Castleman, K. R. (1979) *Digital Image Processing*, Prentice Hall International, Englewood Cliffs, NJ.
- Erhardt, A., Zinser, G., Komitowski, D., and Bille, J. (1985) *Appl. Opt.* **24**, 194–200.
- Tommasi, T., Diaspro, A., and Bianco, B. (1993) *Signal Proc.* **32**, 357–366.

18. Preza, C., Miller, M. I., Thomas, L. J., Jr., and McNally, J. G. (1992) *J. Opt. Soc. Am. A* **9**, 219–228.
19. Carrington, W. A., Fogarty, K. E., and Fay, F. S. (1990) in *Non-Invasive Techniques in Cell Biology* (Foskett and Grinstein, Eds.), A. R. Liss, New York.
20. Holmes, T. J. (1988) *J. Opt. Soc. Am. A* **5**, 666–673.
21. Conchello, J. A., and McNally, J. G. (1996) *Proc. IS&T/SPIE Symp. Electronic Imaging Sci. Technol. San Jose, CA* **2655**, 199–208.
22. Conchello, J. A., and McNally, J. G. (1996) in *Three Dimensional Microscopy: Image Acquisition and Processing* (Cogswell, C. J., Kino, G., and Wilson, T.), Vol. III, *Proc. SPIE* **2655**, 199–208.
23. Conchello, J. A., Markham, J., and McNally, J. G. (1997) *Microw. Microanal.* **3**, 375–376.
24. Joshi, S., and Miller, M. I. (1993) *J. Opt. Soc. Am. A* **10**, 1078–1085.
25. Avinash, G. B. (1995) *Zool. Stud.* **34(Suppl. 1)**, 185–185.
26. Holmes, T. J., Bhattacharyya, S., Cooper, J. A., Hinzl, D., Krishnamurthi, V., Lin, W., Roysam, B., Szarowski, D. H., and Turner, J. N. (1995) in *Handbook of Biological Confocal Microscopy* (Pawley, J. B., Ed.), pp. 389–402, Plenum, New York.
27. Heinlein, M., Padgett, H. S., Gens, J. S., Pickard, B. G., Casper, S. J., Epel, B. L., and Beachy, R. N. (1998) *Plant Cell* **10**, 1107–1120.
28. Gibson, F. S., and Lanni, F. (1991) *J. Opt. Soc. Am. A* **8**, 1601–1613.